HAL
open science

Temperature dependence of the collision-induced absorption band of O2 near 1.27 μm

Samir Kassi, Salah Guessoum, Juan Acosta Abanto, Ha Tran, Alain Campargue, Didier Mondelain

To cite this version:

Samir Kassi, Salah Guessoum, Juan Acosta Abanto, Ha Tran, Alain Campargue, et al.. Temperature dependence of the collision-induced absorption band of O2 near 1.27 μm. Journal of Geophysical Research: Atmospheres, 2021, 126 (13), pp.e2021JD034860. 10.1029/2021JD034860 . hal-03752053

HAL Id: hal-03752053

https://hal.science/hal-03752053v1

Submitted on 16 Aug 2022

HAL is a multi-disciplinary open access archive for the deposit and dissemination of scientific research documents, whether they are published or not. The documents may come from teaching and research institutions in France or abroad, or from public or private research centers.

L'archive ouverte pluridisciplinaire **HAL**, est destinée au dépôt et à la diffusion de documents scientifiques de niveau recherche, publiés ou non, émanant des établissements d'enseignement et de recherche français ou étrangers, des laboratoires publics ou privés.

Temperature dependence of the collision-induced absorption band of O_2 near 1.27 µm

S. Kassi[a], S. Guessoum[a], J. C. Acosta Abanto[a], H. Tran[b], A. Campargue[a], D. Mondelain[a*]

[a] Univ. Grenoble Alpes, CNRS, LIPhy, 38000 Grenoble, France.

[b] Laboratoire de Météorologie Dynamique, IPSL, CNRS, Sorbonne Université, École normale supérieure, PSL Research University, École polytechnique, F-75005 Paris, France

[*]Corresponding author: Didier Mondelain (didier.mondelain@univ-grenoble-alpes.fr)

Key Points:

- The temperature dependence of the CIA of the 1.27 µm O_2 band is measured by highly sensitive cavity ring down spectroscopy.
- Comparison with previous calculations shows similar temperature dependence for O_2-N_2 CIA while for O_2 CIA large differences are visible.
- When comparing to experimental data of Maté et al. (1999) for O_2-air CIA, a similar shape and temperature dependence are observed.
- Temperature coefficients are provided to account for the variation of the O_2 CIA at 1.27 µm in the range of the atmospheric temperatures.

Abstract

The 1.27 µm O_2 band is called upon to be used more and more for air-mass determination from ground-based and space-borne atmospheric spectra because of its advantages compared to the A-band at 0.76 µm. For this purpose, it is important to well characterize not only the narrow absorption lines but also the strong underlying broad collision-induced absorption (CIA) structure and its temperature dependence. Spectra of O_2 and of O_2 in N_2 were recorded by cavity ring down spectroscopy (CRDS) at 271 K and 332 K, with the help of a newly developed temperature regulated cell. The quality of the spectra allowed determining the small variations (at the few percent level) of the $B_{O_2-O_2}$, $B_{O_2-N_2}$ and B_{O_2-air} binary coefficients with temperature. Together with the binary coefficients at 297 K reported previously, they allow characterizing the temperature dependence of the O_2 CIA at 1.27 µm in atmospheric conditions. The obtained results are compared with previous measurements by Fourier transform spectroscopy (FTS) and recent theoretical calculations. In the wings of the pure O_2 CIA, an increase with temperature is observed in agreement with calculations but contrary to the latter, a decrease is observed near the maximum of the CIA band. The temperature dependence is found in good agreement with the theoretical $B_{N_2-O_2}$ values and the experimental B_{O_2-air} values derived from the FTS measurements. Binary coefficients integrated over the entire band show almost no variation with temperature for O_2-N_2 and a small increase for pure O_2, in agreement with the theoretical predictions.

1. Introduction

Thanks to its constant volume mixing ratio of 0.2095 in the Earth's atmosphere (Goody & Yung, 1989), oxygen is used as a proxy to determine sounded air- masses (Long et al., 2010; Washenfelder et al., 2006; Wunch et al., 2011). Up to very recently, the A-band of O_2 centered at 0.76 µm was preferred to retrieve air-masses from space borne instruments. The weaker $a\ ^1\Delta_g - X\ ^3\Sigma_g^-(0-0)$ band near 1.27 µm was only used by ground-based instruments as those of the Total Carbon Column Observing Network (TCCON) (Washenfelder et al., 2006) even if it presents specific advantages. First, being weaker, the 1.27 µm band shows less saturated lines and reduced line-mixing effects compared to the A-band. Second, its spectral proximity with the CO_2 and CH_4 absorption bands near 1.60 µm and 1.66 µm, respectively, allows reducing uncertainties due to the aerosol scattering which spectrally varies depending on location of the sounded air-column (Bertaux et al., 2018).

Until recently, the strong mesosphere/stratosphere airglow produced by O_3 photo-dissociation limited the use of the 1.27 µm band to ground-based remote sensing. But, Bertaux et al. (2018) and Sun et al. (2018) managed to accurately model this effect rendering this band suitable for space-borne observations. Hence, as a comparative test, both the A- and 1.27 µm bands will be covered by the

MicroCarb satellite dedicated to the accurate determination of CO_2 in the troposphere, that should be launched in 2021 (CNES, 2018). In order to achieve a targeted accuracy on the column-averaged CO_2 mole fraction better than 1 ppm (i.e. 0.3% in relative), an accurate derivation of the dry air column is mandatory. To achieve this goal, the rovibronic lines of the 1.27 µm band must be accurately characterized together with the underlying CIA. This is all the more crucial as about half of the total O_2 absorption of the 1.27 µm band is due to the CIA for 1 amagat of air.

Note that the heat balance of the Earth's atmosphere is affected by the O_2 CIA bands which overall contribute to absorption of about 1 Wm^{-2} (Zender, 1999). About 22% of this contribution (integrated between 5000 and 30000 cm^{-1}) is due to the 1.27 µm band.

O_2 bands could also be used as a marker of the oxygenic photosynthesis (Misra et al., 2014, Schwieterman et al., 2018) and bring constraints on the atmospheric pressures of the Earth's like exoplanets. Hence, Misra et al., (2014) showed that atmospheric pressures could be retrieved from pure bound and quasi-bound O_2 complexes in the near infrared for a certain range of pressures and O_2 volume mixing ratios. They also calculated that the CIA of the 1.27 µm band should be detectable in some cases during transit transmission spectroscopy by the future *James Webb Space Telescope* (Gardner et al., 2006).

In the $a\ ^1\Delta_g - X\ ^3\Sigma_g^-(0-0)$ band centered near 1.27 µm, the electric dipole rovibronic transitions are forbidden by both spin ($S = 1 \nrightarrow 0$) and spatial ($g \nrightarrow g$) selection rules. Monomer absorption is thus due to the (weak) spin–orbit-allowed magnetic dipole transitions and even weaker electric quadrupole transitions and $(1-1)$ hot band transitions (Gordon et al., 2010; Leshchishina et al., 2010). These monomer lines are superimposed to the CIA continuum coming from the transient electric dipole induced by collisions of O_2-O_2 and O_2-N_2 molecules (Gordon et al., 2017; Solomon et al., 1998). Note that in our atmosphere, the absorption coefficient integrated over an absorption line is proportional to the O_2 density, ρ_{O_2}, while the CIA involves a self-component proportional to ρ_{O_2} squared and a foreign component proportional to $\rho_{O_2}\rho_{N_2}$.

The CIA of the 1.27 µm band has been studied experimentally with grating or Fourier transform (FT) spectrometers at room temperature and below since more than 60 years (Badger et al., 1965; Blickensderfer et al., 1969; Chagas et al., 2002; Cho 1963; Dianov-Klokov, 1964; Ketelaar, 1955; Maté et al., 1999; McKellar et al., 1972; Smith et al., 1999; Tabisz et al., 1969), but only a few studies (Chagas et al., 2002; Maté et al., 1999; Newnham and Ballard, 1998; Smith and Newnham, 2000) reported cross-sections with reasonable signal-to-noise ratio because of the quite weak CIA absorption. For this reason,

all these previous studies used long absorption path lengths and sample pressures at atmospheric pressures or above.

Recently, cavity enhanced absorption techniques like cavity-ring-down spectroscopy (CRDS) have been applied to the O_2 CIA measurements (Karman et al., 2018; Mondelain et al., 2019) and more generally to the continua measurements (see for example Campargue et al., 2016 and references herein; Lechevallier et al., 2018; Mondelain et al., 2017 and references herein; Richard et al., 2017). These techniques were found particularly suitable as they provide both a high sensitivity and a high baseline stability of the spectra.

The present work follows our CRDS study of the 1.27 µm CIA at room temperature (Mondelain et al., 2019) in support of the *MicroCarb* satellite mission. Here, we focus on the temperature dependence of the CIA *i.e.* of the $B_{O_2-O_2}$, $B_{O_2-N_2}$, and B_{O_2-air} binary absorption coefficients. For this purpose, a temperature regulated CRDS cell has been developed and spectra of pure O_2 and of O_2 in N_2 were recorded at 271 K and 332 K between 7550 and 8360 cm^{-1}. Overall, the set of measurements at three temperatures allows for the determination of the temperature dependence of the O_2 CIA at 1.27 µm in the range of the atmospheric temperatures. This study, together with the recent works devoted to the absorption lines (Konefał et al., 2020; Tran et al., 2020), will help to meet the spectroscopic accuracy requirements of the *MicroCarb* satellite mission. In the next part (Part 2), the experimental set-up and the adopted experimental strategy are presented. The spectra analysis and retrieval of the binary absorption coefficients are presented in Part 3. The comparison of the obtained temperature dependence with those from FTS measurements of Maté et al. (1999) and calculations of Karman et al. (2018) is discussed in Part 4 and perspectives are drawn up in Part 5.

2. Experimental set-up

The high sensitivity and baseline stability of the continuous wave CRDS technique (Berden et al., 2000; Maity et al., 2021; Romanini et al., 1997) have been largely demonstrated during the last years (Campargue et al., 2016 and references herein; Kassi et al., 2012). Reader is referred to (Kassi et al., 2012; Mondelain et al., 2019) for the presentation of our CRDS setup. For this project, we developed a temperature regulated high finesse cavity (HFC) (**Figure 1**) using the circulation of a coolant as adopted in Ghysels et al. (2017).

2.1. The temperature regulated high finesse cavity

Two high reflectivity mirrors from Layertec (*R*>99.99% over the 1170 nm-1370 nm range), separated by 500 mm, were placed inside a stainless steel tube (700 mm long, 63 mm external diameter) fitted with two receptacle flanges at both ends. Outer flanges, housing anti-reflective and wedged

windows, are bolted to the receptacle with a Viton o-ring ensuring the tightness. This aspect is inherited from previous liquid nitrogen cooled setup (Kassi et al., 2008) and high pressure CRDS setup (Kassi et al., 2015). The gas is therefore free to circulate around the mirrors.

The tube was thermalized thanks to two counter-propagating copper coils through which a cooling fluid flows. A non-flammable, low vapor pressure silicone oil has been chosen as the heat transfer fluid. Its temperature was regulated using a deported refrigerated/heating circulator (model Corio 1000F from Julabo). Thanks to the counter-propagating arrangement, temperature gradients were averaged out, ensuring a uniform temperature of the cell envelope. Thanks to this highly symmetric conception, thermo-mechanical gradients were essentially self-compensated allowing for preservation of the optical alignment, which was done at room temperature, after several temperature cycles from -20 to +60°C.

To further homogenize the gas temperature and limit convection, a copper tube (1 mm thick, 30 mm outer diameter), resting on two isolating shims, was installed between the two high reflectivity mirrors to closely surround the probed gas. Four 3-wires 1000 Ω platinum temperature sensors (⅓ DIN class B from -50°C to 150°C) were installed at the surface of the copper tube to determine the sample temperature. Maximum gradients of 0.3 K and 0.5 K along the HFC axis were measured at 270 K and 332 K, respectively, which reads as 0.2% relative. A satisfactory long term stability of the temperature was observed. Over several weeks, internal copper tube temperature fluctuated between 331.50 K and 331.65 K and between 270.1 K and 270.8 K for 333.15 K and 268.15 K coolant set points, respectively.

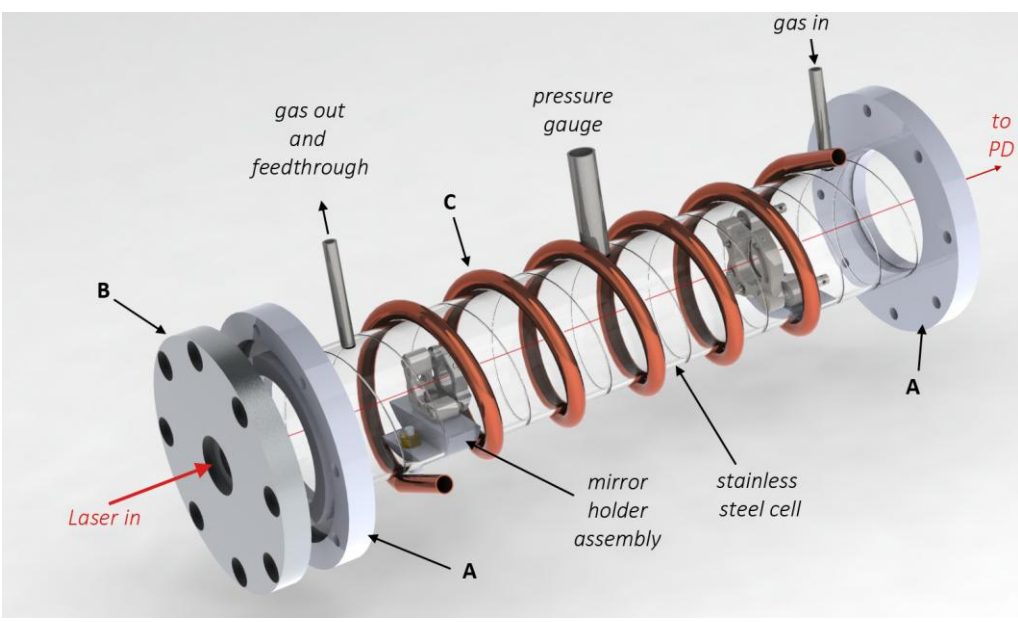

Figure 1. Scheme of the temperature regulated cavity ring down cell developed for the present study. Here *A*, *B* and *C* correspond to the receptacle and outer flanges and to the copper coil, respectively. The CRD setup is enclosed in a thermalized chamber. The gas is free to circulate all around the mirrors.

The temperature is adjusted by circulating temperature regulated fluid in two contra-propagating copper coils. For clarity, the second coil and the internal copper tube (see text) are not shown and the length of the cell is not to scale. One of the mirror is actually hold on a PZT actuator (not shown) allowing for cavity length dithering. Electrical wires of the Pt1000 probes and PZT are passing through the gas tubing.

2.2. Spectra acquisition

Eleven distributed feed-back (DFB) fibered laser diodes and one external cavity laser diode (ECDL) were used as CRDS light sources. The 7550-7920 cm^{-1} range was covered with the DFB diode lasers; each of them allowing for a 30 cm^{-1} spectral coverage. The ECDL was used to cover the 7920-8360 cm^{-1} range. The emitted light wavenumber was measured during each scan by sending a part of the beam to a wavelength meter (Bristol 621-A IR or HighFinesse WSU7-IR). Following a cw-CRDS scheme (Morville et al. 2004), the cavity length was dithered with a PZT element supporting the output mirror. With the DFB laser diodes, the spectra were recorded with a spectral step equal to 3×10^{-3} cm^{-1} or 5×10^{-3} cm^{-1} depending on the gas pressure/density. At each spectral step of a scan, several ring down events were acquired, fitted with an exponential fit and averaged, providing an averaged RD time, τ. With the ECDL, in order to increase the scan speed, no effort was done to discipline it. Only its grating was scanned, leading to spectral steps of typically of 0.1 cm^{-1}, induced by the laser cavity modes. The RD events and corresponding wavenumbers were recorded *on the fly*, when scanning the ECDL over its entire emission range, taking about 2 hours per spectrum.

For each laser diode and for the ECDL, the procedure consisted in recording in static regime a series of spectra corresponding to two consecutive spectra with the cell filled by pure O_2 (99.9999% purity) or a mixture of O_2+N_2 (with an O_2 relative concentration of 20.965±0.044% (2σ); O_2+N_2>99.9999% provided by Air Liquide), framed by two argon spectra (99.9999% purity) for the base line determination (**Figure 2**). The cell was entirely pumped between the gas changes. As this procedure was time consuming (typically 5 hours for the four spectra recorded for each diode), contrary to our previous CIA study at room temperature (Mondelain et al., 2019), only one pressure was recorded for a given laser diode. In addition to the superposition of the two argon spectra recorded for one diode, the baseline stability was checked with the overlap spectral range between two consecutive laser diodes as illustrated in **Figure 2**. For pure O_2, the cell was filled at different pressures from 300 Torr to 750 Torr depending of the CIA amplitude, while for the O_2+N_2 mixture, a pressure of 700 Torr was adopted. These gas pressures were measured with a heated absolute capacitance manometer (model AA02A from MKS instruments; 1000 mbar full scale; accuracy: 0.12% of the reading).

The extinction coefficient, $\alpha(\nu)$, corresponds to the difference between the loss rates for the cell filled with pure O_2 or O_2+N_2 gas mixture, $n/c\tau$ and with a non-absorbing gas (i.e. argon in our case), $n_{Ar}/c\tau_0$,

$$\alpha(\nu) = \frac{n}{c\tau(\nu)} - \frac{n_{Ar}}{c\tau_0(\nu)} \tag{1}$$

where c is the speed of light and n and n_{Ar}, are the refractive indexes of the absorbing gas and argon, respectively. $1/c\tau_0$ is related to the reflectivity of the mirrors, R, and the cavity length, L_{cav}:

$$\frac{n_{Ar}}{c\tau_0(\nu)} = \frac{1-R(\nu)}{L_{cav}} \tag{2}$$

The RD time, τ_0, varied from 90 µs at 7870 cm^{-1} to 67 µs at 7550 cm^{-1} for the cell filled with argon. The measured extinction coefficient is the sum of contributions from the O_2 monomer lines, the O_2 CIA and Rayleigh scattering.

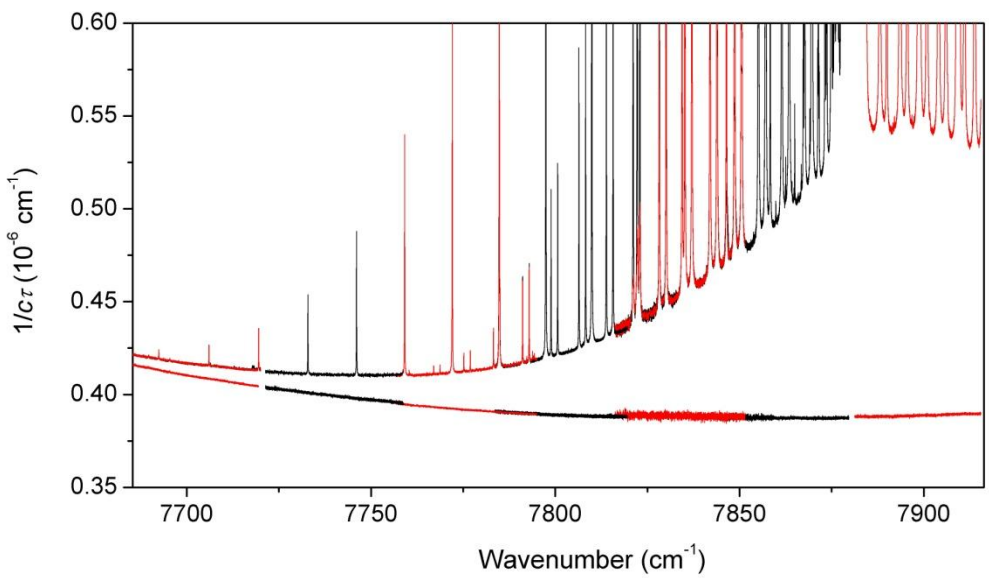

Figure 2. CRDS spectra recorded with different DFB laser diodes (red/black solid lines) for the O_2+N_2 mixture (upper spectra) and argon (lower spectra) at a total pressure of 700 Torr and a temperature of 271.2 K. The argon baseline is mostly due to the mirror reflectivity curve and includes a small Rayleigh scattering contribution. Note the good superposition of the baselines recorded at different days.

Spectra were recorded by scanning the DFB laser diode temperature leading to minimum detectable absorption coefficient (evaluated as the *rms* of the baseline fluctuation), α_{min}, between 2×10^{-10} cm^{-1} and 5×10^{-10} cm^{-1}, for the cell filled with argon, depending on the DFB laser diode. The excess of noise

observed on **Figure 2** between 7820 cm^{-1} and 7860 cm^{-1} was due to the low emitted power of one of the DFB laser diode.

3. Spectra analysis

3.1. Retrieval of the binary coefficients

First, the spectrum baseline due to the mirror losses has to be subtracted to the oxygen (or N_2+O_2 mixture) spectra. After removal of some water vapor absorption lines (present as an impurity at the ppm level in argon), the argon spectra were fitted with a second order polynomial function for each DFB laser diode and a fourth order polynomial for the ECDL. After this baseline correction, the small contribution due to Rayleigh scattering was considered and removed. The Rayleigh scattering cross-sections of Ar and O_2 being very close (Thalman et al., 2014; Thalman et al., 2017), its impact on the extinction coefficient is very small (~3×10^{-11} cm^{-1} at 700 Torr and 331K) which leads to a negligible correction on the $B_{O_2-O_2}$measurements. In case of air, the difference with Ar is more important and leads to a linear variation increasing from 3.9×10^{-10} cm^{-1} at 7690 cm^{-1} to 5.0×10^{-10} cm^{-1} at 8150 cm^{-1} for a pressure of 700 Torr and a temperature of 270 K (Thalman et al., 2014; Thalman et al., 2017). This weak effect was taken into account in the determination of the $B_{O_2-N_2}$, binary coefficients.

The remaining absorption coefficient is expressed by:

$$\alpha_{O_2}(\nu) = B_{O_2-O_2}(\nu)\rho_{O_2}^2 + M_{O_2}(\nu)\rho_{O_2} \tag{3}$$

for pure O_2, and by:

$$\alpha_{O_2+N_2}(\nu) = B_{O_2-O_2}(\nu)\rho_{O_2}^2 + M_{O_2}(\nu)\rho_{O_2} + B_{O_2-N_2}(\nu)\rho_{O_2}\rho_{N_2} \tag{4}$$

for the N_2+O_2 mixture.

Where ρ are densities in amagat, $B_{O_2-O_2}$and $B_{O_2-N_2}$are the binary collision absorption coefficients in cm^{-1} $amagat^{-2}$. $M_{O_2}(\nu)\rho_{O_2}$ is the local monomer contribution due to the 1.27 µm band of O_2 that was generated using the most recent spectroscopic data [see (Tran et al., 2021) and references therein]. A speed dependent Nelkin-Ghatak profile was used for these intense lines and a Voigt profile for the others, with a cutoff value of ±5 cm^{-1} from the line center. It was also necessary to include the line mixing effect for the *Q*- and *R*-branches region near 7890 cm^{-1} (Tran et al., 2020). This calculated line contribution was subtracted from the spectrum as illustrated on **Figure 3**. Note that the obtained residuals included in **Figure 3** show some large values which have an experimental origin: the very strong absorption due to the O_2 lines leads to very short ring down times and a low level of photons exiting the HFC and thus a high noise level.

The ideal gas law was applied to calculate the densities as the deviation from this law, due to the second virial coefficient, does not exceed 0.06% in the worst case. Due to desorption from the gas cell, water vapor absorption lines were observed in some spectra at 332 K and were removed using a Voigt fit

of their profile (the corresponding relative concentration of water vapor was typically of few ppm). $B_{O_2-O_2}$ coefficients derived from the oxygen spectra (Eq. 3) were used to subtract the O_2-O_2 contribution from the spectra of the N_2+O_2 mixture and derive the $B_{O_2-N_2}$ coefficients (Eq. 4). As illustrated in **Figure 3** for the N_2+O_2 mixture , the O_2-O_2 and N_2-O_2 contributions are on the same order of magnitude near the band maximum.

The following procedure, illustrated on the right panel of **Figure 3**, was used to provide smooth curves for the binary coefficients *versus* the wavenumber. After calculation of the uncertainties of the binary coefficients, as described below, the data points with the strongest uncertainties (i.e. at the location of the absorption lines), were removed. The entire "cleaned" CIA band was then divided into a few spectral intervals (typically ~150 cm^{-1} wide) over which a polynomial fit was performed. The concatenated fit results were then interpolated with a 1 cm^{-1} spectral step.

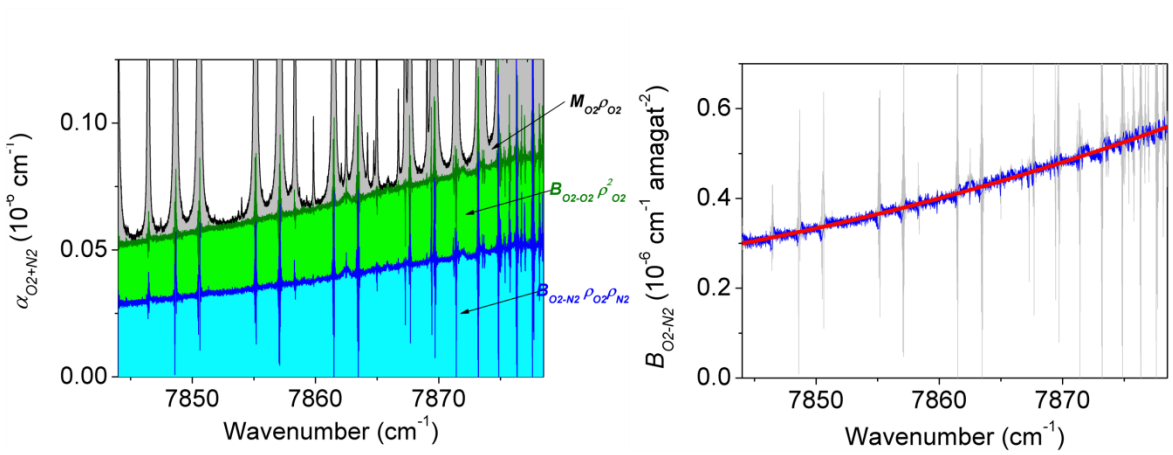

Figure 3. Retrieval of the binary coefficients

Left panel: Different contributions to the absorption coefficient, $\alpha_{O_2+N_2}(\nu)$, measured with the DFB laser diode centered at 1270 nm for a mixture of N_2+O_2 at a total pressure of 700 Torr and a temperature of 331.6 K,

Right panel: Retrieved binary absorption coefficient, $B_{O_2-N_2}$. Refer to the text and Eq. (4) for the different notations. Data point before (grey solid line) and after (blue solid line) data cleaning using the calculated uncertainties are shown together with the result of the fit to the cleaned data corresponding to the recommended $B_{O_2-N_2}$ values (red solid line).

Figure 4 presents an overview of the obtained values of the $B_{O_2-O_2}$ and $B_{O_2-N_2}$ coefficients at 270.5 K and 331.6 K, as provided in the *Supplementary material*.

For atmospheric applications, it is convenient to introduce the B_{O_2-air} coefficient defined by:

$$\alpha_{CIA}(\nu) = B_{O_2-air}(\nu)\rho_{O_2}\rho_{air} \tag{5}$$

where ρ_{air} is the dry air density. The relative concentrations of nitrogen, oxygen and argon in dry air are 78.08, 20.95 and 0.93 %, respectively. The O_2 CIA induced by argon is expected to be very close to that due to nitrogen (Karman et al., 2018). Thus, the B_{O_2-air} values computed as:

$$B_{O_2-air} = 0.2095 B_{O_2-O_2} + (1 - 0.2095) B_{O_2-N_2} \quad (6)$$

are provided as *Supplementary Material* at both temperatures.

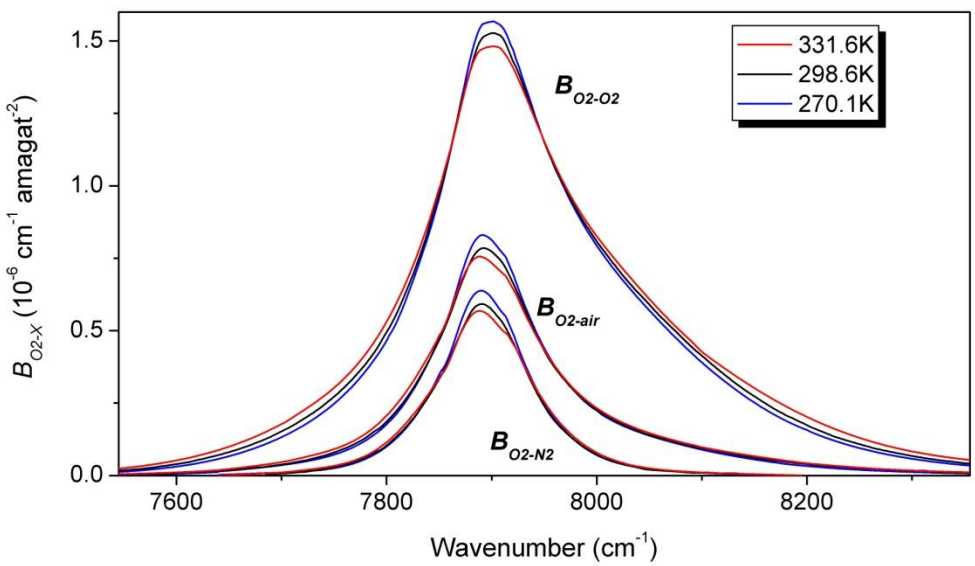

Figure 4. Recommended binary coefficients obtained in this work at 270.1 K and 331.6 K and in (Mondelain et al., 2019) at room temperature.

We have gathered in **Figure 4**, the binary coefficients obtained in this work at 270.1 K and 331.6 K with the results at room temperature reported in (Mondelain et al., 2019). Let us note the consistency of the results of the two studies performed with different CRDS set ups (for instance the length of the CRDS cell used at room temperature was 140 cm to be compared to 50 cm in the present recordings). Although the changes of the CIA shape with temperature are relatively weak, the room temperature curves are systematically intermediate between the 270.1 K and 331.6 K curves. The main variations are observed at the center of the band with a decrease of the binary coefficients with the temperature (maximum variation of 5.7% between 270.1 K and 331.6 K). An opposite behavior occurs in the wings of the pure O_2 CIA.

Using the three temperature values at disposal, the $B_{O_2-X}(\nu_i)$ values can be plotted *versus T* (*X*= O_2, N_2 and air). At each spectral step, ν_i, a mostly linear dependence with the temperature is observed over the 270-331 K interval (**Figure 5** left panel). The corresponding slope $(dB/dT)_{O_2-X}(\nu_i)$ was obtained from a linear fit of the $B_{O_2-X}(\nu_i)$ values at the three temperatures. The frequency dependence of the *dB/dT* is presented on the right panel of **Figure 5**. As expected, the strongest (negative) temperature

coefficients are located near the band maximum at 7900 cm^{-1} for both O_2-O_2 and O_2-N_2. In the wings, both O_2-O_2 and O_2-N_2 coefficients increase with temperature but the effect is more pronounced for O_2-O_2. A small asymmetry of the *dB/dT* profiles can be noted for the different curves.

In the Supplementary Material, we provide for each CIA (O_2-O_2, O_2-N_2, O_2-air), the binary coefficients at 271, 297 and 332 K and the corresponding temperature dependence coefficients and estimated uncertainties. A sample of the Supplementary Material is presented in **Table 1.**

Table 1. Sample of the Supplementary material provided for B_{O_2-air}.
Experimental CRDS B_{O_2-air} binary coefficients obtained from this work (at 271 K and 332 K) and from Mondelain et al. (2019) at 297 K. Values between parenthesis are estimated error bars given in the unit of the last quoted digit.

Spectral step (cm^{-1})	B_{O_2-air}			dB_{O_2-air}/dT
	271K	*297K*	*332K*	(10^{-6} cm^{-1} $amagat^{-2}$ K^{-1})
7920	*0.6980(138)*	*0.6667(50)*	*0.6464(109)*	*-6.59(41)×10^{-4}*
7921	*0.6889(134)*	*0.6588(50)*	*0.6398(109)*	*-6.18(40)×10^{-4}*
7922	*0.6784(131)*	*0.6509(49)*	*0.6332(108)*	*-5.56(35)×10^{-4}*
7923	*0.6680(128)*	*0.6429(49)*	*0.6266(107)*	*-4.94(30)×10^{-4}*
7924	*0.6584(127)*	*0.6349(49)*	*0.6188(107)*	*-4.46(29)×10^{-4}*
7925	*0.6488(126)*	*0.6271(48)*	*0.6108(106)*	*-4.00(26)×10^{-4}*
7926	*0.6390(126)*	*0.6190(48)*	*0.6027(106)*	*-3.70(22)×10^{-4}*
7927	*0.6290(125)*	*0.6109(48)*	*0.5946(105)*	*-3.41(17)×10^{-4}*
7928	*0.6195(124)*	*0.6027(47)*	*0.5866(105)*	*-3.18(15)×10^{-4}*
7929	*0.6101(124)*	*0.5943(47)*	*0.6464(109)*	*-2.98(13)×10^{-4}*
7930	*0.6008(123)*	*0.5859(47)*	*0.5711(104)*	*-2.79(12)×10^{-4}*

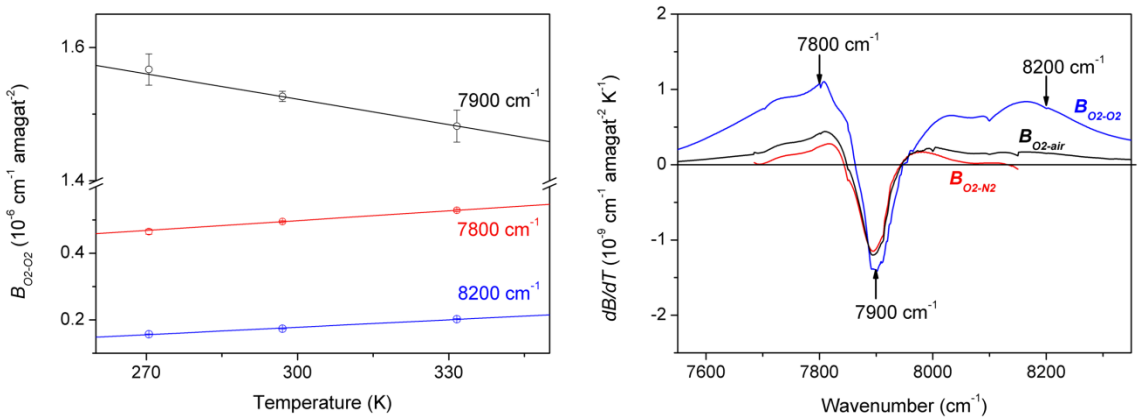

Figure 5. Temperature dependence of the binary coefficients.

Left panel: Example of the variation of the experimental binary coefficient, $B_{O_2-O_2}$, with temperature at 7800, 7900 and 8200 cm^{-1}. Experimental values at 297 K were taken from (Mondelain et al., 2019).

Right panel: Fitted temperature coefficients, *dB/dT*, of $B_{O_2-X}(\nu_i)$ with *X*= O_2, N_2 and air.

3.2. Error budget

Uncertainties on the retrieved binary absorption coefficients have been calculated with the propagation of error approach using Eqs. (3) and (4) and assuming uncorrelated variables.

The base line stability was systematically checked for each series of spectra by comparing the argon spectra recorded before and after the absorbing gas spectra (see **Figure 2**). Stability of 5×10^{-10} cm^{-1} or below was achieved except for two series where a degraded stability of ~1×10^{-9} cm^{-1} was observed. These values were adopted as the uncertainties on α_{O_2} and $\alpha_{O_2+N_2}$. Uncertainties on the densities, calculated from the pressure gauge and temperature sensor accuracies together with gas stated purity and concentrations, are typically around 0.15%. To estimate the uncertainty coming from the subtracted monomer contribution we applied the method proposed in (Ptashnik et al., 2007). As explained above, we removed the data points with the largest uncertainties, corresponding to the location of the absorption lines so that this latter contribution becomes marginal for the "cleaned" data points.

The resulting absolute uncertainties (1σ) of the different binary coefficients are included in the *Supplementary Material*. Over a large part of the absorption band, uncertainties better than 3% and 5% have been achieved for O_2-O_2 CIA and O_2-N_2 CIA, respectively. Note that, for the uncertainties on *dB/dT*, given by the linear fit, the uncertainties on the binary coefficients were not included leading to an underestimation on that reported uncertainties.

4. Comparison to literature

Let us discuss our CRDS results in comparison to the previous measurements of Maté et al. (1999), and to the theoretical calculations of Karman et al. (2018). Maté et al. (1999) used an FT spectrometer with high densities gas samples (between 1 and 10 amagat) at three temperatures: 253, 273, and 296 K with an absorption path length of 84.05 m. The theoretical approach of Karman et al. (2018) used analytical models and numerical quantum scattering calculations. The spin-orbit and exchange mechanisms have been identified to break the spin symmetry in the studied collision complexes (Karman et al., 2017; Karman et al., 2018). Through quadrupole induction, these two mechanisms lead to transition dipole moments responsible of the CIA of the considered $a\ ^1\Delta_g - X\ ^3\Sigma_g^-(0-0)$ band of O_2. The FTS and calculated O_2 CIA cross-sections of the considered 1.27 µm band of O_2 are provided in the updated version of the CIA section of the HITRAN database (Karman et al., 2019).

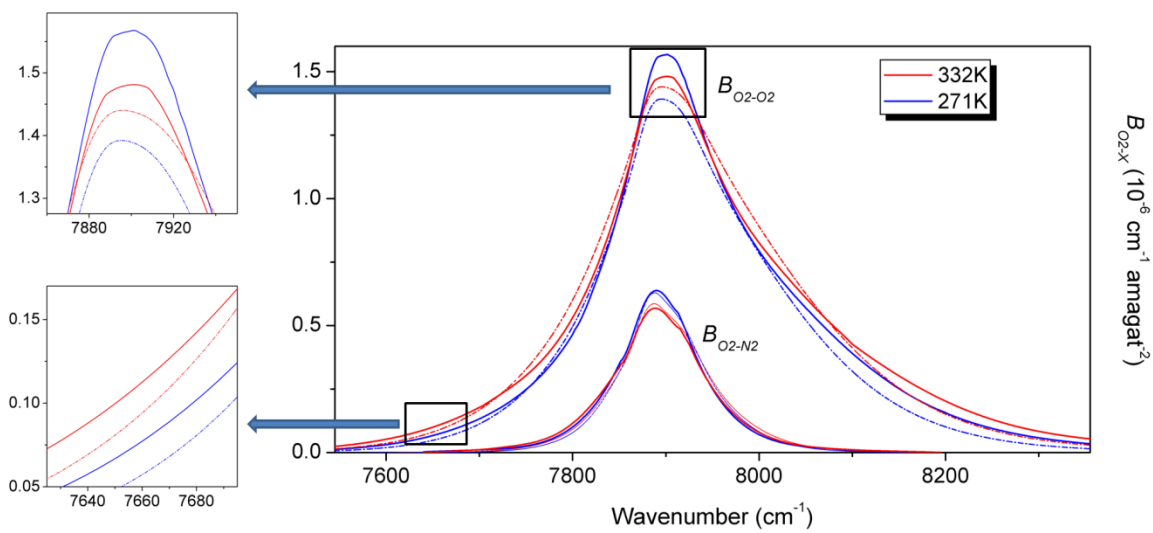

Figure 6. Comparison of the binary coefficients obtained experimentally at 270.1 K and 331.6 K in this work with the theoretical values derived from Karman et al. (2018) at 271K and 332 K for $B_{O_2-O_2}$ and 275 K and 323 K for $B_{O_2-N_2}$. Note that room temperature data are not shown for clarity reasons.

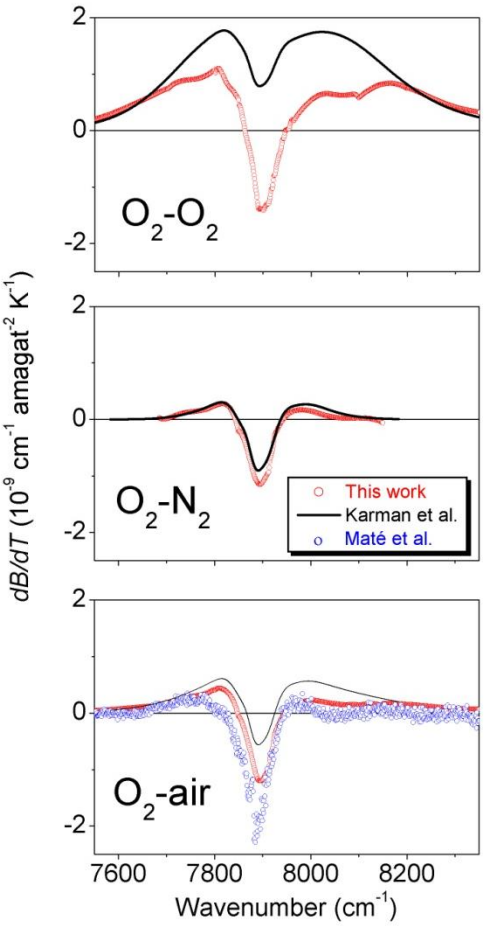

Figure 7. Comparison of the temperature dependence of the $B_{O_2-O_2}(\nu_i)$ (upper panel), $B_{O_2-N_2}(\nu_i)$ (middle panel) and $B_{O_2-air}(\nu_i)$ (lower panel) binary coefficients derived from CRDS measurements (This work), FTS measurements (Maté et al., 1999) and theoretical calculations (Karman et al., 2018).

Figure 6 presents an overview comparison of our binary coefficients with the calculated values from Karman et al., (2018) at 271 K and 332 K. At the scale of the overview, a general agreement in observed. For a more detailed comparison, it is worth comparing the *dB/dT* derivatives as displayed on **Figure 7**. In the same way as done for the CRDS values, *dB/dT* values were derived, for each wavenumber value, from a linear fit of the *B* values of Maté et al. (1999) (at 253, 273 and 296 K) and Karman et al. (2018) (at 271, 296 and 332 K for $\boldsymbol{B_{O_2-O_2}}$and 275, 298 and 323 K for $\boldsymbol{B_{O_2-N_2}}$ and $\boldsymbol{B_{O_2-air}}$).

Even if slightly more negative temperature coefficients are obtained around the band center in the case of Maté et al. (1999), the FTS and CRDS results for air are close (Maté et al. (1999) did not report binary coefficients for O_2-O_2 and O_2-N_2 at temperatures other than 296 K). Considering the different

experimental techniques, range of pressure values used in the two studies and the limited temperature dependence of the CIA, the achieved agreement provides a mutual validation and can be considered as very satisfactory.

Compared to Karman et al. (2018) a very good agreement is observed for the O_2-N_2 CIAs. It is interesting to mention that only the spin-orbit mechanism is present for the O_2-N_2 collision complexes leading to the conclusion that this mechanism is well theoretically characterized in Karman et al. (2018) in the case of O_2-N_2.

The situation is less satisfactory for the O_2-O_2 temperature dependence. Far from the center, the temperature evolution is also well predicted by calculations, but, closer to the center, large differences are visible. In particular, according to the calculations, the O_2-O_2 CIA absorption is predicted to increase for all the wavenumber values while our measurements reveal a significant negative temperature dependence between 7860 cm^{-1} and 7950 cm^{-1}. In the case of pure O_2 CIA, the exchange mechanism contributes to the CIA in addition to the spin-orbit mechanism. As shown in Fig. 4 of Karman et al. (2018), the spin-orbit mechanism leads to a relatively narrow band shape dominating in the center of the O_2-O_2 CIA band while the exchange mechanism leads to a broad contribution dominating in the wings, with an equivalent contribution of the two mechanisms around 20 cm^{-1} from the center. Our observations indicate that the positive temperature dependence of the exchange mechanism is overestimated by the calculations and/or that the negative temperature dependence of the spin-orbit mechanism (around the center) is underestimated for O_2-O_2 CIA.

Table 2 lists the CRDS, FTS and calculated integrated band intensities, S_{O_2-X} (X= O_2, N_2 or air), corresponding to the integration of the fitted binary coefficients B_{O_2-X} over the entire spectral range. The obtained values are compared in **Figure 8**. Note that, in order to reproduce quantitatively the experimental results of Maté et al. (1999), scaling factors have been applied at room temperature to the theoretical line shapes corresponding to the exchange and spin-orbit mechanisms (Karman et al., 2018). As already noted in Mondelain et al. (2019), a very satisfactory overall agreement is found when comparing our data to the FTS values. Even if some small shape differences are observed, the mutual compensation of deviations leads to very close integrated band intensities.

In the case of O_2-N_2, according to calculations, the integrated intensity, $S_{O_2-N_2}$, is mostly independent of the temperature with a mean value around 70×10^{-6} cm^{-2} $amagat^{-2}$ which falls within the error bars of the FTS and CRDS values.

In the case of O_2-O_2, the calculated integrated $B_{O_2-O_2}$ coefficient is predicted to increase significantly with the temperature (about 15% over ~60 K). This is about twice the increase rate measured by CRDS while Maté et al. did not evidence any significant variation between 253 and 296 K.

	Temperature K	$S_{O_2-O_2}$ 10^{-6} cm^{-2} amagat^{-2}	$S_{O_2-N_2}$ 10^{-6} cm^{-2} amagat^{-2}	S_{O_2-air} 10^{-6} cm^{-2} amagat^{-2}
This work	271.1	349.2(60)	73.3(25)	131.2(33)
Mondelain et al. (2019)	297.0	358.8(21)[a]	71.1(37)	131.4(29)[a]
This work	331.6	375.0(60)	71.6(25)	134.5(33)
Maté et al. (1999)	253.0	349.9(9)	73.7(20)	131.7(15)
	273.3	347.3(10)	67.8(25)	126.5(19)
	296.2	349.9(16)	67.9(36)	127.1(27)
Karman et al. (2018)	271/275/275[b]	321.1[c]	70.6	121.3
	296/298/298[b]	341.6[c]	70.9	124.9
	332/323/323[b]	373.7[c]	71.2	129.1

Table 2. Integrated binary coefficients derived from this work and from the literature. The numbers in parenthesis correspond to the 1σ uncertainties in unit of the last digit. The associated uncertainties were obtained by integrating the binary coefficients plus and minus their uncertainties.

[a] The given values of $S_{O_2-O_2}$ and S_{O_2-air} are smaller by 0.9 and 0.5 % compared than the value reported in Table 1 of Mondelain et al. (2019), respectively, because, for comparison to the present work, the integration was limited to the 7546-8354 cm^{-1} interval, narrower than the 7515-8466 cm^{-1} considered in Mondelain et al. (2019),

[b] The temperatures correspond respectively to $S_{O_2-O_2}$, $S_{O_2-N_2}$ and S_{O_2-air}.

[c] Obtained using the *Supplementary Material* of Karman et al. (2018) and extended values given by T. Karman over the 7483-8482 cm^{-1} spectral range.

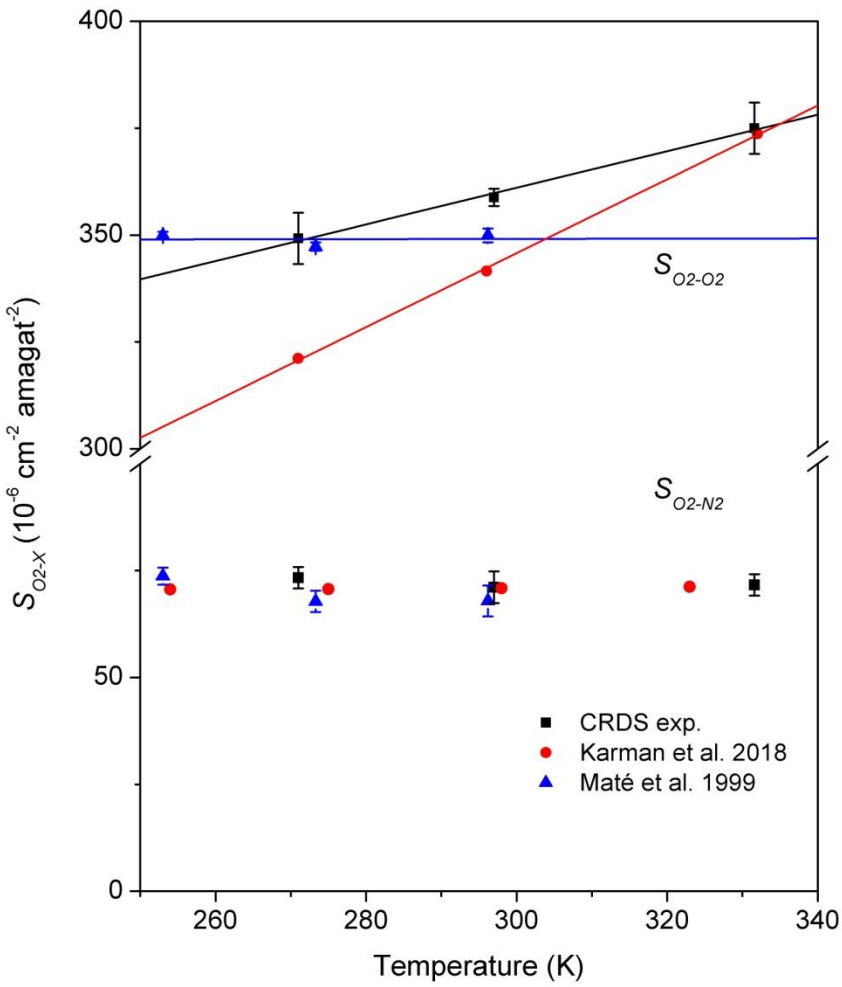

Figure 8. Evolution of the experimental and theoretical integrated intensities of the $S_{O_2-N_2}$ and $S_{O_2-O_2}$ *versus* temperature.

It is important to mention that over the 270-332 K temperature range, the theoretical binary coefficients of Karman et al. (2018) evolves quasi-linearly with the temperature similarly to what we observe experimentally. When considering a larger temperature interval (e. g. between 200 K and 350 K), the calculations predict a quadratic dependence with temperature over some spectral ranges. We estimate that our experimental $B_{O_2-Air}(\nu_i)$ binary coefficients should be safely linearly extrapolated over the 250 K-350 K temperature range.

5. Conclusion and perspectives

Spectra of pure O_2 and N_2-O_2 mixture were recorded at 271 K and 332 K over the 7550 – 8360 cm^{-1} spectral range thanks to a highly sensitive and stable cavity ring down spectrometer based on a newly developed temperature regulated high finesse optical cavity. The performances of the developed CRDS set-up, in particular its long term stability, allowed to accurately determine the small variation (a few %) of the CIAs with temperature. The $B_{O_2-O_2}$, $B_{O_2-N_2}$ and B_{O_2-air} binary absorption coefficients of the CIA retrieved from these spectra and the ones obtained at room temperature from our previous work (Mondelain et al., 2019) will allow to account for the variation of the CIA in the temperature range of the Earth's atmosphere.

Comparison to the calculations of Karman et al. (2018) shows a similar temperature dependence for $B_{O_2-N_2}$while for $B_{O_2-O_2}$ significant differences are noted near the band center. The reported results provide constraints on the scaling factor of the line shapes for the spin-orbit and exchange mechanisms and could help to better estimate the exchange-induced dipole which has quite large uncertainty.

Our B_{O_2-air} coefficients are found in good agreement with results of Maté et al. (1999) obtained by FTS in different pressure conditions (up to 10 atm, while our CRDS spectra where recorded at pressures ranging between 300 and 700 Torr). Integrated binary coefficients over the entire band show almost no variation with temperature for O_2-N_2 CIA and an increase with temperature for pure O_2 CIA in qualitative agreement with the same quantities derived from calculations of Karman et al. (2018).

As *MicroCarb* instrument will use the B4 band between 7800-7912 cm^{-1} to retrieve the surface pressure and then normalize the computed CO_2 column concentration, the impact of our new O_2 CIA data set on these quantities will be investigated using high signal-to-noise ratio and high resolution TCCON spectra with well-known pressure, temperature, humidity conditions and instrument characteristics. For that, spectra will be calculated with the Spectroscopic Parameters And Radiative Transfer Evaluation (SPARTE) chain (Armante et al., 2016), a calibration/validation chain, used to compare ground-based and space-borne observations. The direct radiative transfer calculations will be done by the 4A/OP code selected for the calibration/validation activities of *MicroCarb*.

It could also be useful to update the study of Zender (1999) on the solar absorption of oxygen collision complexes based on the new data set provided in this work and in Mondelain et al. (2019), for the CIA of the 1.27 µm band, and in the updated version of HITRAN (Karman et al., 2019). This will allow refining the radiative forcing due to oxygen collision pairs.

In a recent study, Baranov et al., (2012) and Hartmann et al. (2018) shown that the CIA of N_2 is importantly enhanced by water vapor. In this context, the magnitude of the O_2 CIA induced by atmospheric water vapor in wet atmospheres should also be investigated.

Acknowledgements

This work was supported by CNES in the frame of the *MicroCarb* project. Authors also want to thank T. Karman for providing them unpublished calculations extending the CIA spectral range. DM wants to thank S. Béguier for writing the program to calculate the temperature coefficients.

Data Availability Statement

The base line corrected CRDS spectra used in this work are available under: https://zenodo.org/badge/DOI/10.5281/zenodo.4562331.svg

References

Armante R., Scott N., Crevoisier C., Capelle V., Crepeau L., Jacquinet N., & Chédin A. (2016). Evaluation of spectroscopic databases through radiative transfer simulations compared to observations. Application to the validation of GEISA 2015 with IASI and TCCON. *J Mol Spectrosc*, 327, 180-192. doi:10.1016/j.jms.2016.04.004

Badger, R. M., Wright, A. C., & Whitlock, R. F. (1965). Absolute intensities of the discrete and continuous absorption bands of oxygen gas at 1.26 and 1.065 µm and the radiative lifetime of the 11g state of oxygen. *Journal of Chemical Physics*, 43, 4345–4350.

Baranov, Y. I.,, Buryak, I. A., Lokshtanov, S. E., Lukyanchenko, V. A. & Vigasin, A. A. (2012). H_2O-N_2 collision-induced absorption band intensity in the region of the N_2 fundamental: *ab initio* investigation of its temperature dependence and comparison with laboratory data. *Phil. Trans. R. Soc. A*, 370, 2691–2709. doi:10.1098/rsta.2011.0189

Berden, G., Peeters, R., & Meijer, G. (2000). Cavity Ring-Down Spectroscopy: Experimental schemes and applications. *International Review in Physical Chemistry*, 19, 565–607. doi:10.1080/014423500750040627.

Bertaux, J.-L., Hauchecorne, A., Lefèvre, F., Jouglet, D., Blanot, L., Bréon, F.-M., et al. (2018) Use of the 1.27 µm O_2 absorption band for CO_2 and methane estimates in nadir viewing from space: Potential and application to Microcarb. *Geophysical Research Abstracts*, 20, EGU2018-14935, EGU General Assembly 2018.

Blickensderfer, R. P., & Ewing, G. E. (1969). Collision-induced absorption Spectrum of Gaseous Oxygen at Low Temperatures and Pressures. I. The $^1\Delta_g$–$^3\Sigma^-_g$ System. *Journal of Chemical Physics*, 51, 873-883.

Campargue, A., Kassi, S., Mondelain, D., Vasilchenko, S., & Romanini, D. (2016). Accurate laboratory determination of the near-infrared water vapor self-continuum: A test of the MT_CKD model. *Journal of Geophysical Research: Atmospheres*, 121, D13180. doi:10.1002/2016JD025531.

Chagas, J. C. S., Newnham, D. A., Smith, K. M., & Shine, K. P. (2002). Impact of new measurements of oxygen collision-induced absorption on estimates of short-wave atmospheric absorption. *Quarterly Journal of the Royal Meteorological Society*, 128, 2377–2396. doi:10.1256/qj.01.159

Goody, R. M., & Yung, Y. L. (1989). *Atmospheric Radiation Theoretical Basis*, 2nd ed., New York, Oxford University Press.

Cho, C. W., Allin, E. J., & Welsh, H. L. (1963). Effect of high pressures on the infrared and red atmospheric absorption band systems of oxygen. *Canadian Journal of Physics*, 41, 1991–2002.

CNES (2018) : https://microcarb.cnes.fr/en

Dianov-Klokov, V. I. (1964). Absorption spectrum of oxygen at pressures from 2 to 35 atm in the region from 12600 to 3600 Å. *Optics and Spectroscopy* (EnglishTranslation), 16, 224–227.

Gardner, J. P., Mather, J.C., Clampin, M., Doyon, R., Greenhouse, M. A., Hammel, H. B., et al. (2006). The James Webb Space Telescope. *Space Science Reviews*, 123: 485–606. doi:10.1007/s11214-006-8315-7

Ghysels, M., · Liu, Q., Fleisher, A. J., & Hodges, J. T. (2017). A variable-temperature cavity ring-down spectrometer with application to line shape analysis of CO_2 spectra in the 1600 nm region. *Applied Physics B*, 123,124. doi:10.1007/s00340-017-6686-y

Gordon, I. E., Kassi, S., Campargue, A., & Toon, G. C. (2010). First identification of the $a\ ^1\Delta_g - X\ ^3\Sigma_g^-(0-0)$ electric quadrupole transitions of oxygen in the solar and laboratory spectra. *Journal of Quantitative Spectroscopy & Radiative Transfer*, 111, 1174-1183. doi:10.1016/j.jqsrt.2010.01.008

Gordon I. E., Rothman, L. S., Hill, C., Kochanov, R. V., Tan, Y., Bernath, P. F., et al. (2017). The HITRAN2016 Molecular Spectroscopic Database. *Journal of Quantitative Spectroscopy & Radiative Transfer*, 203, 3-69. doi:10.1016/j.jqsrt.2017.06.038

Hartmann, J.-M., Boulet, C., Tran D.D., Tran, H. (2018) Effect of humidity on the absorption continua of CO_2 and N_2 near 4 µm: Calculations, comparisons with measurements, and consequences for atmospheric spectra. *J. Chem. Phys.*, 148, 054304. doi:10.1063/1.5019994)

Karman, T., van der Avoird, A., & Groenenboom, G. C. (2017). Line-shape theory of the $X\ ^3\Sigma_g^- - a\ ^1\Delta_g, b\ ^1\Sigma_g^+$ transitions in O_2–O_2 collision-induced absorption. *Journal of Chemical Physics*, 147, 084307. doi:10.1063/1.4990662

Karman, T., Koenis, M. A. J., Banerjee, A., Parker, D. H., Gordon, I. E., van der Avoird, A., et al. (2018). O_2−O_2 and O_2−N_2 collision-induced absorption mechanisms unraveled. *Nature Chemistry*, 10, 549–554, doi:10.1038/s41557-018-0015

Karman, T., Gordon I. E., van der Avoird A., Baranov Y. I., Boulet C., Drouin B. J., et al. (2019). Update of the HITRAN collision-induced absorption section. *Icarus*, 328, 160–175. doi:10.1016/j.icarus.2019.02.034

Kassi, S., Gao, B., Romanini, D. & Campargue, A. (2008). The near infrared (1.30–1.70 µm) absorption spectrum of methane down to 77 K. Phys. *Chem. Chem. Phys.* 10, 4410–4419. doi:10.1039/B805947K

Kassi, S. & Campargue, A. (2012). A. Cavity ring down spectroscopy with 5×10^{-13} cm^{-1} sensitivity. *Journal of Chemical Physics*, 137, 234201, doi:10.1063/1.4769974.

Kassi, S., Campargue, A., Mondelain, D., & Tran, H. (2015). High pressure Cavity Ring Down Spectroscopy: Application to the absorption continuum of CO_2 near 1.7 µm. *Journal of Quantitative Spectroscopy & Radiative Transfer*. 167, 97–104. doi:10.1016/j.jqsrt.2015.08.014

Ketelaar, J. A. A. (1955). La transition triplet-singlet dans l'oxygene sous pression. *Nuovo Cimento*, II, suppl., ser X, 3, 763–765.

Konefał M., Kassi S., Mondelain D., & Campargue A. (2020). High sensitivity spectroscopy of the O_2 band at 1.27 µm: (I) pure O_2 line parameters above 7920 cm^{-1}. *Journal of Quantitative Spectroscopy & Radiative Transfer* 241, 106653. doi:10.1016/j.jqsrt.2019.106653

Lechevallier, L., Vasilchenko, S., Grilli, R., Mondelain, D., Romanini, D., & Campargue A. (2018). The water vapour self-continuum absorption in the infrared atmospheric windows: new laser measurements near 3.3 and 2.0 µm. *Atmospheric Measurements Techniques*, 11, 2159–2171. doi:10.5194/amt-11-2159-2018.

Leshchishina, O., Kassi, S., Gordon, I. E., Rothman, R. L., Wang, L., & Campargue A. (2010). High sensitivity CRDS of the $a\ ^1\Delta_g - X\ ^3\Sigma_g^-(0-0)$ band of oxygen near 1.27 µm: extended observations, quadrupole transitions, hot bands and minor isotopologues, *Journal of Quantitative Spectroscopy & Radiatiative Transfer*, 111, 2236-2245. doi:10.1016/j.jqsrt.2010.05.014.

Long, D.A., Havey, D.K., Okumura, M., Miller, C.E., & Hodges, J.T. (2010) O_2 A-band line parameters to support atmospheric remote sensing. *Journal of Quantitative Spectroscopy & Radiatiative Transfer*, 111, 2021-2036. doi:10.1016/j.jqsrt.2010.05.011

Maity, A., Maithani, S., & Pradhan M. (2021). Cavity Ring-Down Spectroscopy: Recent Technological Advancements, Techniques, and Applications. *Anal. Chem.*, 93, 388−416. doi:10.1021/acs.analchem.0c04329.

Maté, B., Lugez, C., Fraser, G. T., & Lafferty W. J. (1999). Absolute intensities for the O_2 1.27 µm continuum absorption. *Journal of Geophysical Research: Atmospheres*, 104, D30585. doi:10.1029/1999JD900824.

McKellar, A. R. W., Rich, N. R., & Welsh H. L. (1972). Collision-induced vibrational and electronic spectra of gaseous oxygen at low temperatures. *Canadian Journal of Physics*, 50, 1–9.

Mendonca, J., Strong, K., Wunch, D., Toon, G. C., Long, D. A., Hodges, J. T., et al. (2018) Improving the Retrieval of XCO_2 from Total Carbon Column Network Solar Spectra. *Atmospheric Measurement Techniques*. 124, 414–423. doi:10.5194/amt-2018-62

Misra, A., Meadows, V., Claire, M., & Crisp, D. (2014). Using Dimers to Measure Biosignatures and Atmospheric Pressure for Terrestrial Exoplanets. *Astrobiology*, 14, 68-86. doi:10.1089/ast.2013.0990

Mlawer, E. J., Clough, S. A., Brown, P. D., Stephen, T. M., Landry, J. C., Goldman, A., & Murcray, F. (1998). Observed atmospheric collision-induced absorption in near infrared oxygen bands. *Journal of Geophysical Research: Atmospheres*, 103, D3859. doi:10.1029/97JD03141

Mondelain, D., Campargue, A., Čermák, P., Gamache, R.R., Kassi, S., Tashkun, S.A., & Tran, H. (2017). The CO_2 absorption continuum by high pressure CRDS in the 1.74 µm window. *Journal of Quantitative Spectroscopy & Radiative Transfer* 203, 530–537. doi:10.1016/j.jqsrt.2017.02.019

Mondelain, D., Kassi, S., & Campargue, A. (2019). Accurate laboratory measurement of the O_2 collision-induced absorption band near 1.27 µm. *J. Geophys. Res.: Atmospheres* 124,414–423. doi:10.1029/2018JD029317

Morville, J., Romanini, D., Kachanov, A. A., & Chenevier, M. (2004). Two schemes for trace detection using cavity ring down spectroscopy. *Applied Physics B*, 78, 465–476. doi:10.1007/s00340-003-1363-8

Newnham, D. A., & Ballard, J. (1998). Visible absorption cross sections and integrated absorption intensities of molecular oxygen (0_2 and 0_4), *Journal of Geophysical Research: Atmospheres*, 103, D22, 28,801. doi:10.1029/98JD02799

Ptashnik I. V. (2007). Evaluation of suitable spectral intervals for near-IR laboratory detection of water vapour continuum absorption. *Journal of Quantitative Spectroscopy & Radiative Transfer*. 108, 146–160. doi:10.1016/j.jqsrt.2007.03.011.

Richard, L., Vasilchenko, S., Mondelain, D., Ventrillard, I., Romanini, D., & Campargue, A. (2017). Water vapor self-continuum absorption measurements in the 4.0 and 2.1 μm transparency windows, *Journal of Quantitative Spectroscopy & Radiatiative Transfer*, 201, 171–179. doi:10.1016/j.jqsrt.2017.06.037

Romanini, D., Kachanov, A. A., Sadeghi, N., & Stoeckel, F. (1997). CW cavity ring down spectroscopy, *Chemical Physics Letters*, 264, 316–322. doi:10.1016/S0009-2614(96)01351-61997.

Schwieterman, E. W., Olson, S. L.,Reinhard, C. T., Ridgwell, A., Kane, S., Meadows, V. S., & Lyons, T. W. (2018). Exoplanet Biosignatures: A Review of Remotely Detectable Signs of Life *Astrobiology*, 18, doi:10.1089/ast.2017.1729

Smith, K. M., & Newnham, D. A. (1999). Near-infrared absorption spectroscopy of oxygen and nitrogen gas mixtures, *Chemical Physics Letters*, 308, 1–6. doi:10.1016/S0009-2614(99)00584-9

Smith, K. M., & Newnham, D. A. (2000). Near-infrared absorption cross sections and integrated absorption intensities of molecular oxygen (O_2, O_2-O_2, and O_2-N_2). *Journal of Geophysical Research*, 105, 7383-7396. doi:10.1029/1999JD901171

Solomon, S., Portmann, R. W., Sanders, R. W., & Daniel, J. S. (1998) Absorption of solar radiation by water vapour, oxygen, and related collision pairs in the earth's atmosphere, *Journal of Geophysical Research: Atmospheres*, 103, D4, 3847–3858. doi:10.1029/97JD03285

Sun, K., Gordon, I. E., Sioris, C. E., Liu, X., Chance, K., & Wofsy, S. C. (2018). Re-evaluating the use of O_2 $a^1\Delta_g$ band in the spaceborne remote sensing of greenhouse gases, *Geophysical Research Letters*, 45, 5779–5787. doi:10.1029/2018GL077823.

Tabisz, G. C., Allin, E. J., & Welsh, H. L. (1969). Interpretation of the visible and near-infrared absorption spectra of compressed oxygen as collision-induced electronic transitions. *Canadian Journal of Physics*, 47, 2859-2871.

Thalman, R., Zarzana, K., Tolbert, M. A., & Volkamer, R. (2014). Rayleigh scattering cross-section measurements of nitrogen, argon, oxygen and air, *Journal of Quantitative Spectroscopy & Radiatiative Transfer*, 147, 171–177. doi:10.1016/j.jqsrt.2014.05.030.

Thalman, R., Zarzana, K., Tolbert, M. A., & Volkamer, R. (2017). Erratum to "Rayleigh scattering cross-section measurements of nitrogen, argon, oxygen and air" J. Quant. Spectrosc. Radiat. Transfer 147 (2014) 171-177, *Journal of Quantitative Spectroscopy & Radiatiative Transfer*, 189, 281-282. doi:10.1016/j.jqsrt.2016.12.014

Tran, D.D., Tran, H., Vasilchenko, S., Kassi, S., Campargue A., & Mondelain, D. (2020). High sensitivity spectroscopy of the O_2 band at 1.27 μm: (II) air-broadened line profile parameters, *Journal of Quantitative Spectroscopy & Radiative Transfer*, 240, 106673. doi:10.1016/j.jqsrt.2019.106673

Tran, D. D., Delahaye, T., Armante, R., Hartmann, J.-M., Mondelain, D., Campargue, A., Fleurbaey, H., Hodges, J. T., Tran, H. (2021). Validation of spectroscopic data in the 1.27 μm spectral region by comparisons with ground-based atmospheric measurements. *Journal of Quantitative Spectroscopy & Radiative Transfer*, 261, 107495. doi:10.1016/j.jqsrt.2020.107495

Washenfelder, R. A., Toon, G. C., Blavier, J.-F., Yang, Z., Allen, N. T., Wennberg, P. O., et al. (2006), Carbon dioxide column abundances at the Wisconsin Tall Tower site. *Journal of Geophysical Research: Atmospheres*, 111, D22305. doi:10.1029/2006JD007154.

Wunch, D., Toon, G. C., Blavier, J.-F. L., Washenfelder, R. A., Notholt, J., Connor, B. J., et al. (2011) The Total Carbon Column Observing Network. *The Philosophical Transactions of the Royal Society A*, 369, 2087–2112. doi:10.1098/rsta.2010.0240

Zender, C. S. (1999). Global climatology of abundance and solar absorption of oxygen collision complexes. *Journal of Geophysical Research: Atmospheres,* 104**,** D20, 24471–24484. doi:10.1029/1999JD900797